Received: 16 July 2022 | Accepted: 9 October 2022

DOI: 10.1002/nme.7144

RESEARCH ARTICLE

WILEY

Discrete exterior calculus for photonic crystal waveguides

Sanna Mönkölä | **Joona Räty**

Faculty of Information Technology, University of Jyväskylä, Jyväskylä, Finland

Correspondence
Sanna Mönkölä, Faculty of Information Technology, University of Jyväskylä, Jyväskylä, Finland.
Email: sanna.monkola@jyu.fi

Abstract

The discrete exterior calculus (DEC) is very promising, though not yet widely used, discretization method for photonic crystal (PC) waveguides. It can be seen as a generalization of the finite difference time domain (FDTD) method. The DEC enables efficient time evolution by construction and fits well for nonhomogeneous computational domains and obstacles of curved surfaces. These properties are typically present in applications of PC waveguides that are constructed as periodic structures of inhomogeneities in a computational domain. We present a two-dimensional DEC discretization for PC waveguides and demonstrate it with a selection of numerical experiments typical in the application area. We also make a numerical comparison of the method with the FDTD method that is a mainstream method for simulating PC structures. Numerical results demonstrate the advantages of the DEC method.

KEYWORDS

discrete differential forms, discrete exterior calculus, finite difference time domain method, photonic band gap, photonic crystal waveguide

1 | INTRODUCTION

Photonic crystals (PCs) are periodic structures used to control the propagation of light. There are two basic structures of PCs: dielectric rods in the air substrate and air holes in dielectric material. Silicon provides a high dielectric contrast with air and is a common material used as dielectrics in PC devices and experimental research studies. A PC waveguide can be constructed by removing a row of inhomogeneities (scatterers, dielectric rods, or air holes) from the PC slab. Since the light is electromagnetic radiation, it scatters from the inhomogeneities in the PC, at certain frequencies the wave is vanished by destructive interference and the light propagation is prevented. Such frequencies form a photonic bandgap (PBG). With frequencies outside of the PBG the light can propagate through the PC. The light of the PBG frequency range can propagate through the waveguide. The PBG is dependent on the geometrical properties of the PC, including the lattice constant that describes the distance between the center of neighboring scatterers.

Because of the nanoscale size, geometrical structure, and material constraints, PCs with inhomogeneities in three-dimensions are more challenging to fabricate than the two-dimensional ones.[1] On the other hand, three-dimensional structures that are long and uniform in the out-of-plane direction can be presented as two-dimensional models. That is why the research interests are still focused on two-dimensional models. Computational tests with numerical models form a fast and cost-efficient way to test and design PCs. The numerical PC models are presented as propagation of electromagnetic waves in heterogeneous domain or coupled systems involving two or more materials. Frequency

domain computations give information about the PBG[2,3] and with time domain simulations it is possible to analyze the time evolution of light waves before constructing physical PC products.[4]

In order to be of practical use, the computational approaches are required to give accurate results in a reasonable computing time. The finite difference time domain (FDTD) method has become the standard tool to run computer simulations in the field of study. However, the complex geometry of the PC models is challenging to simulate accurately and efficiently with the conventional FDTD method. That is why the boundary element method (BEM)[5] or hybrid methods relying on the geometric flexibility of the finite element methods (FEM) have been applied.[6-8] The main drawback of the FEM-based simulation is that in time domain it typically requires the inversion or factorization of a sparse matrix at each time step.[9]

The discrete exterior calculus (DEC) can be seen as a differential form based generalization of finite difference methods, including the FDTD. The DEC enables such grid structures that can handle complex domains. Since only inversion of a diagonal matrix is required at each timestep, it also provides efficient time-stepping.[10] The method is pioneered in electromagnetic simulations by Bossavit and Kettunen,[11] while the groundwork presented by Marsden's group was applied in computer vision and image processing[12] and delivered the PyDEC software library.[13] During the last decade, the DEC has been applied to, for example, elastostatics,[14] electromagnetics,[15] quantum mechanics,[16,17] and flow problems.[18] Chen and Chew[2] applied the method for PC band structure computations in frequency domain. They also have shown that the method provides self-consistent and self-contained discrete electromagnetic theory.[19] Recently, Kettunen et al.[20] have advanced the method with higher order Whitney forms and Toshniwal and Hughes[21] have introduced isogeometric discrete differential forms. Despite the wide number of considered application areas and numerical experiments there exist only a few examples of wave propagation in heterogeneous domain in which the time-dependent problem is discretized with the DEC. These include electromagnetic scattering by objects such as hexagonal ice crystals or spherical particles randomly distributed into the surrounding media.[10,22] In the ice crystal simulations, the object has been considered to be large compared to the wavelength, while spherical particles were small compared to the wavelength.

In this article, we simulate a PC structure of an array of cross-sections of dielectric rods in the air substrate. Although our examples concentrate on demonstrating the feasibility of the DEC as a discretization scheme for PC waveguides, it is worth mentioning a few application areas benefiting from such computational tools. The models considered in our numerical studies form a basis in the design of optical logic gates and photonic circuits.[23,24] More sophisticated, hydrogel-based, PCs are important applications in the development of noninvasive optical glucose sensors.[25] PCs also provide future prospects in photovoltaic solar cell technologies.[26]

The rest of this article is organized as follows. In Section 2, we present the mathematical model, first in the vector field notation and then in the language of differential forms. In Section 3, we discretize the differential form presentation in space by the DEC and in time by the conventional leap-frog scheme and consider the boundary conditions at the discrete stage. The numerical tests on transmission conditions, material properties, geometry approximation, mesh refinements strategies, and band gaps of PCs are based on software implemented at the University of Jyväskylä and considered in Section 4. The conclusions are presented in Section 5.

2 | THE MAXWELL EQUATIONS

Time-dependent propagation of electromagnetic waves is presented by the hyperbolic system of the Maxwell equations

$$\varepsilon \frac{\partial \mathbf{E}}{\partial t} - \nabla \times \mathbf{H} = \mathbf{J}_E, \tag{1}$$

$$\mu \frac{\partial \mathbf{H}}{\partial t} + \nabla \times \mathbf{E} = \mathbf{J}_H, \tag{2}$$

$$\nabla \cdot \mathbf{D} = \rho_E, \tag{3}$$

$$\nabla \cdot \mathbf{B} = \rho_H, \tag{4}$$

where $\mathbf{E} = (E_1, E_2, E_3)^T$ and $\mathbf{H} = (H_1, H_2, H_3)^T$ are the electric and magnetic field strengths, ε is the electric permittivity, μ is the magnetic permeability, and $\mathbf{J}_E = (J_{E1}, J_{E2}, J_{E3})^T$ is the current density of the electric charge which is assumed to be divergence free, that is, $\nabla \cdot \mathbf{J}_E = 0$. Respectively, we define the magnetic current density $\mathbf{J}_H = (J_{H1}, J_{H2}, J_{H3})^T$. Electric and magnetic charges are presented by ρ_E and ρ_H, respectively. The electric flux density $\mathbf{D}$, electric field

strength $\mathbf{E}$, magnetic flux density $\mathbf{B}$, and magnetic field strength $\mathbf{H}$ are related by the constitutive equations $\mathbf{D} = \varepsilon\mathbf{E}$ and $\mathbf{B} = \mu\mathbf{H}$. The electromagnetic wave propagates with the angular frequency ω at speed $c(\mathbf{x}) = 1/\sqrt{\mu(\mathbf{x})\varepsilon(\mathbf{x})}$. The wavenumber $\kappa(\mathbf{x}) = \omega/c(\mathbf{x})$ describes how many waves there are for a 2π unit. The corresponding wavelength is given by $\lambda(\mathbf{x}) = 2\pi/\kappa(\mathbf{x}) = c(\mathbf{x})/f$, where $f = \omega/2\pi$ is the frequency. The corresponding time-harmonic problem is considered with

$$\mathbf{E}(\mathbf{x}, t) = \boldsymbol{\mathcal{E}}(\mathbf{x})\exp(-\mathbf{i}\,\omega t), \quad \mathbf{D}(\mathbf{x}, t) = \boldsymbol{\mathcal{D}}(\mathbf{x})\exp(-\mathbf{i}\,\omega t),$$
$$\mathbf{H}(\mathbf{x}, t) = \boldsymbol{\mathcal{H}}(\mathbf{x})\exp(-\mathbf{i}\,\omega t), \quad \mathbf{B}(\mathbf{x}, t) = \mathcal{B}(\mathbf{x})\exp(-\mathbf{i}\,\omega t),$$

where $\mathbf{x} = (x_1, x_2, x_3)^T \in \mathbb{R}^3$ is the spatial variable and $\mathbf{i} = \sqrt{-1}$ is the imaginary unit. To truncate the domain Ω by an absorbing boundary Γ_{ext}, we can use the Silver–Müller boundary condition

$$\mathbf{H}\times\mathbf{n} = -\sqrt{\frac{\varepsilon}{\mu}}(\mathbf{E}\times\mathbf{n})\times\mathbf{n},$$

where $\mathbf{n}$ is the outward pointing normal vector, to complete the circulation along missing dual edges of a boundary vertex. Another choice to restrict ourselves to a finite computational domain is to use a perfectly matched layer (PML).[27]

To simulate dielectric rods in air, we concentrate on transverse magnetic (TM) modes. That is, $\mathbf{E} = (0, 0, E_3)^T$, $\mathbf{H} = (H_1, H_2, 0)^T$, $\mathbf{B} = (B_1, B_2, 0)^T$, $\mathbf{D} = (0, 0, D_3)^T$, $\mathbf{J}_E = (0, 0, J_{E3})^T$, and $\mathbf{J}_H = (J_{H1}, J_{H2}, 0)^T$. Under the circumstances, the differential form representation corresponding to problem (1)–(4) is

$$d\tilde{H} = \frac{\partial\tilde{D}}{\partial t} - \tilde{J}_E, \tag{5}$$
$$d\tilde{E} = -\frac{\partial\tilde{B}}{\partial t} + \tilde{J}_H, \tag{6}$$
$$d\tilde{B} = \tilde{\rho}_H, \tag{7}$$
$$d\tilde{J}_H = \frac{\partial\tilde{\rho}_H}{\partial t}, \tag{8}$$

where d is the exterior derivative, $\tilde{E} = E_3$ is a differential 0-form, $\tilde{H} = H_1dx_1 + H_2dx_2$, $\tilde{B} = B_1dx_2 - B_2dx_1$, and $\tilde{J}_H = J_{H1}dx_2 - J_{H2}dx_1$ are differential 1-forms, and $\tilde{D} = D_3dx_1\wedge dx_2$, $\tilde{J}_E = J_{E3}dx_1\wedge dx_2$, and $\tilde{\rho}_H = \rho_H dx_1\wedge dx_2$ are differential 2-forms, and $\wedge$ is the exterior product (wedge product) operator. The constitutive relations are $\tilde{D} = \star_\varepsilon\tilde{E}$ and $\tilde{B} = \star_\mu\tilde{H}$, where $\star_\varepsilon$ and $\star_\mu$ are permittivity and permeability related Hodge operators mapping a differential p-form to a differential $n-p$ form, where n is the spatial dimension. Respectively, we would have a 0-form $\tilde{H}$, 1-forms $\tilde{E}$, $\tilde{D}$, and $\tilde{J}_E$, and 2-forms $\tilde{B}$ and $\tilde{\rho}_E$ for considering transverse electric (TE) modes.[28] By replacing the time derivative operator $\frac{\partial}{\partial t}$ by a multiplier $-\mathbf{i}\,\omega$, we get the corresponding time-harmonic problem.[19]

3 | DISCRETIZATION

To discretize the computational domain Ω we construct a computational mesh. It is a collection of N_Ω polygonal surface elements Ω_k, $k = 1, \ldots, N_\Omega$, such that $\Omega = \bigcup_{k=1}^{N_\Omega}\Omega_k$. There are N_e edges e_j, $j = 1, \ldots, N_e$, and N_v vertices v_i, $i = 1, \ldots, N_v$, in the mesh. In addition to this (primal) mesh we construct its dual mesh by connecting the nearest circumcenters (see Figure 1). The elements of both the primal and dual mesh can be seen as surfaces bounded by edges bounded by vertices. Thus, we can see a hierarchy of cells such that a vertex is a 0-cell, an edge between two 0-cells is a 1-cell, and a surface surrounded by edges is a 2-cell. For each p-cell in the primal mesh there is a $(2-p)$-cell in the dual mesh. That is, the surface elements Ω_i^* of the dual mesh are dual to the primal vertices v_i and the edges e_j^* of the dual mesh are dual to the primal edges e_j. The dual mesh of a primal mesh constructed of squares is constructed of squares and the dual mesh of a primal mesh constructed of triangles is constructed of hexagons (see Figure 1). The spatial mesh step size, or edge length, is denoted by h. In a nonuniform mesh, we mark the shortest edge length of the primal mesh as $h_{\min}$ and the largest edge length of the primal mesh as $h_{\max}$.

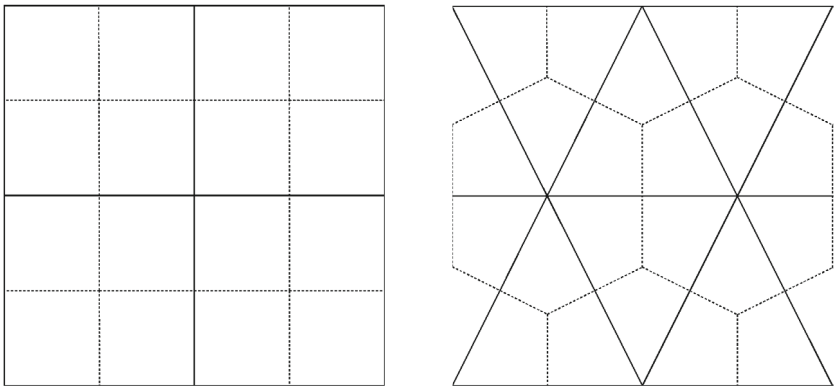

FIGURE 1 Examples of square and triangular primal mesh elements (solid line) and the corresponding dual mesh elements (dashed line)

3.1 | Discrete exterior calculus

The discrete counterpart of a differential p-form is a discrete differential p-form, or p-cochain.[29] The cochains defined on the primal mesh are primal cochains, and the cochains defined on the dual mesh are dual cochains. The primal 0-cochain E, associated with the primal vertices, and the primal 1-cochains B and J_H, associated with the primal edges, are presented as column vectors with components

$$E_i = \int_{v_i} \tilde{E}, \quad B_j = \int_{e_j} \tilde{B}, \quad J_{Hj} = \int_{e_j} \tilde{J}_H, \quad i = 1, \dots, N_v, \quad j = 1, \dots, N_e. \tag{9}$$

Respectively, the dual 1-cochain H, associated with the dual edges, and dual 2-cochains D and J_E, associated with the dual surfaces, are presented as column vectors with components

$$H_j = \int_{e_j^*} \tilde{H}, \quad D_i = \int_{\Omega_i^*} \tilde{D}, \quad J_{Ei} = \int_{\Omega_i^*} \tilde{J}_E, \quad i = 1, \dots, N_v, \quad j = 1, \dots, N_e. \tag{10}$$

The discrete analog of the Hodge star operator presents the constitutive relations at the discrete level. At this point the choice of circumcentric duality between primal and dual mesh is crucial since it provides the diagonality of the discrete Hodge operator that is also a key element of the efficiency of the time-stepping.

We present the discrete Hodge star operator, that may vary with the properties of the medium, as $\star$ and clarify the associated material properties with a subscript. The discrete Hodge star operator $\star_\varepsilon$ maps a primal 0-cochain E to the dual 2-cochain D taking into account permittivity ε. Since $D = \star_\varepsilon E$ should hold, we can construct its inverse, $\star_\varepsilon^{-1}$, as an $N_v \times N_v$ diagonal matrix with components

$$\star_{\varepsilon_{ii}}^{-1} = \frac{E_i}{D_i} = \frac{\int_{v_i} \tilde{E}}{\int_{\Omega_i^*} \tilde{D}} = \frac{E_3(\mathbf{x}_{v_i})}{\int_{\Omega_i^*} \mathbf{D} \cdot d\mathcal{A}} = \frac{E_3(\mathbf{x}_{v_i})}{\varepsilon \mathbf{E} \cdot n_{\Omega_i^*} |\Omega_i^*|} = \frac{1}{\varepsilon |\Omega_i^*|}, \quad i = 1, \dots, N_v, \tag{11}$$

where $d\mathcal{A}$ is the differential vector element of surface area $\mathcal{A}$ normal to the ith dual mesh surface Ω_i^*, $|\Omega_i^*|$ is the surface area of the ith dual mesh surface, and $\mathbf{x}_{v_i}$ gives the coordinates of the vertex v_i. Respectively, we set $H = \star_\nu B$. The discrete Hodge star operator $\star_\nu$ maps a primal 1-cochain B to the dual 1-cochain H taking into account permeability μ, such that $\nu = \mu^{-1}$. It is an $N_e \times N_e$ diagonal matrix with the diagonal components

$$\star_{\nu jj} = \frac{H_j}{B_j} = \frac{\int_{e_j^*} \tilde{H}}{\int_{e_j} \tilde{B}} = \frac{\int_{e_j^*} \mathbf{H} \cdot dl}{\int_{e_j} \mathbf{B} \cdot dl} = \frac{\int_{e_j^*} \mathbf{H} \cdot dl}{\int_{e_j} \mu \mathbf{H} \cdot dl} = \frac{\mathbf{H} \cdot n_{e_j^*} |e_j^*|}{\mu \mathbf{H} \cdot n_{e_j} |e_j|} = \nu \frac{|e_j^*|}{|e_j|}, \quad j = 1, \dots, N_e, \tag{12}$$

where $|e_j^*|$ is the length of the jth dual mesh edge and $|e_j|$ is the length of the jth primal mesh edge.

Discrete exterior derivative $\mathbf{d}_0$ is a boundary operator acting on 0-cochains to produce 1-cochains. It is a sparse $N_e \times N_v$ matrix presenting the incidence number between each edge e_j, $j = 1, \dots, N_e$, and each vertex v_i, $i = 1, \dots, N_v$. The incidence number is 0 if v_i is not a point of e_j. If an edge e_j has a vertex v_i, the value at the jth row and the ith column of the incidence matrix is ± 1, depending on the relative orientation of the edge, that is, whether vertex v_i is the end or start point of edge e_j. Respectively, the discrete exterior derivative $\mathbf{d}_1$ is a $N_\Omega \times N_e$ matrix and it operates on 1-cochains to produce 2-cochains. If the edge e_j is a boundary of face Ω_k, the value at the kth row and the jth column of the incidence matrix is ± 1, depending on the relative orientation between the face and the edge element (see Figures 2 and 3). The other values of the discrete exterior derivative, for the cases edge e_j is not a boundary of face Ω_k, are zeros.

We can summarize the discrete calculus presented above as a diagram

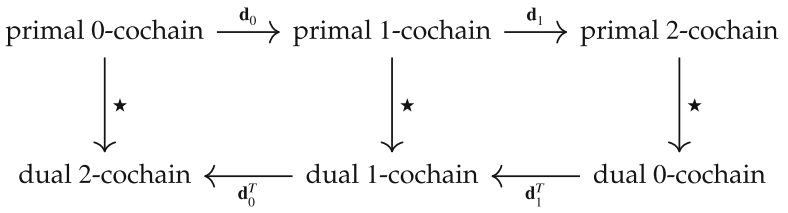

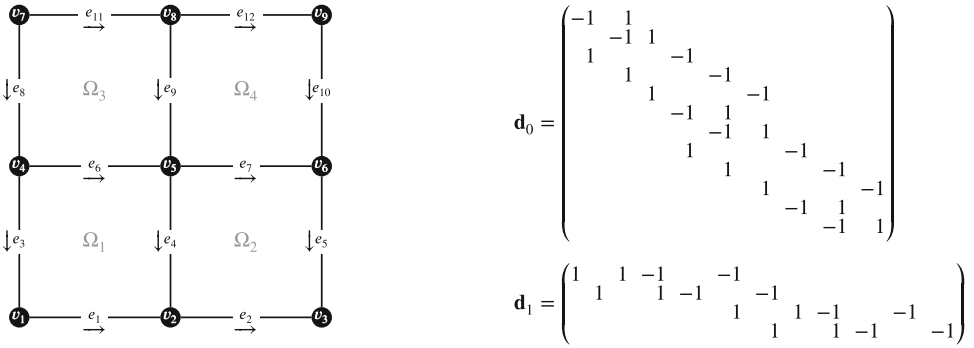

FIGURE 2 An example orientation of the edges e_i, $i = 1, \dots, 12$, and the corresponding discrete exterior derivative matrices $\mathbf{d}_0$ and $\mathbf{d}_1$ for a square primal grid with vertices v_j, $j = 1, \dots, 9$. The counterclockwise orientation of faces Ω_k, $k = 1, \dots, 4$, is assumed to be positive.

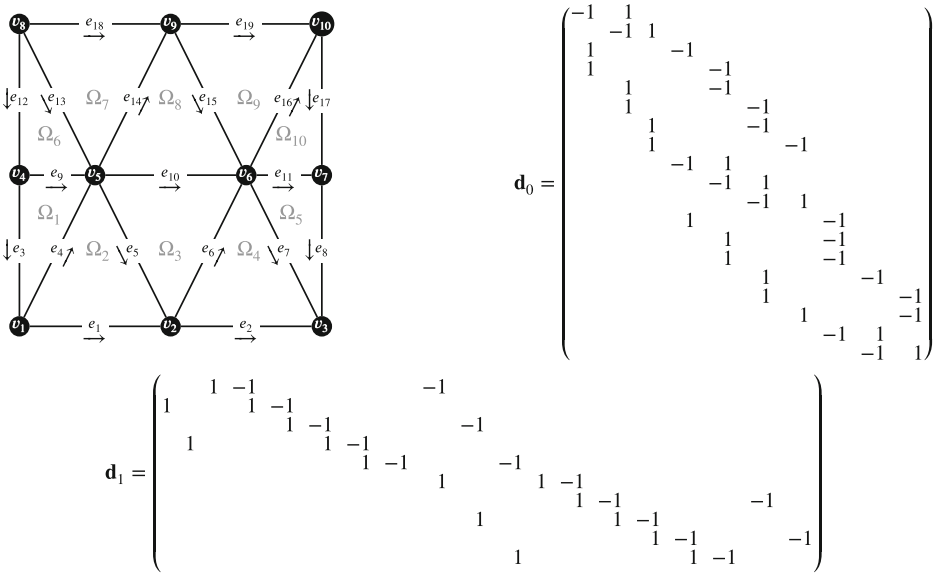

FIGURE 3 An example orientation of the edges e_i, $i = 1, \dots, 19$, and the corresponding discrete exterior derivative matrices $\mathbf{d}_0$ and $\mathbf{d}_1$ for a triangular primal grid with vertices v_j, $j = 1, \dots, 10$. The counterclockwise orientation of faces Ω_k, $k = 1, \dots, 10$, is assumed to be positive.

and present the spatially discretized counterpart of system (5)–(8) as

$$\mathbf{d}_0^T H = \frac{\partial D}{\partial t} - J_E, \tag{13}$$

$$\mathbf{d}_0 E = -\frac{\partial B}{\partial t} + J_H, \tag{14}$$

$$\mathbf{d}_1 B = \rho_H, \tag{15}$$

$$\mathbf{d}_1 J_H = \frac{\partial \rho_H}{\partial t}. \tag{16}$$

3.2 | Leap-frog time-stepping

For time discretization we apply the staggered leap-frog type discretization familiar from the conventional FDTD method. The one-dimensional time domain from $t = t^0$ to $t = t^N$ is divided into time step intervals, each of length Δt. We evaluate Equations (13) and (15) at time $t = t^{n+\frac{1}{2}}$ and Equations (14) and (16) at time $t = t^n$ and approximate the time derivatives by the second order central finite difference method, applied to variables B and E staggered in time, such that

$$\frac{\partial B(t^n)}{\partial t} = \frac{B^{n+\frac{1}{2}} - B^{n-\frac{1}{2}}}{\Delta t}, \quad \frac{\partial E(t^{n+\frac{1}{2}})}{\partial t} = \frac{E^{n+1} - E^n}{\Delta t}, \quad n = 0, \dots, N-1. \tag{17}$$

That is, B is updated at half-integer timesteps, while E is updated at integer timesteps. The initial conditions are set as $B^{-\frac{1}{2}}$ and E^0. To update the primal 1-cochain B, representing the magnetic flux through the mesh edges, and the primal 0-cochain E, representing the electric field located on the mesh vertices, we use the formulas

$$\begin{cases} B^{n+\frac{1}{2}} = B^{n-\frac{1}{2}} - \Delta t(\mathbf{d}_0 E^n - J_H^n), \\ E^{n+1} = E^n + \Delta t \star_\epsilon^{-1} (\mathbf{d}_0^T \star_\nu B^{n+\frac{1}{2}} + J_E^{n+\frac{1}{2}}). \end{cases} \tag{18}$$

The coupled system of equations (18) provides time-stepping that is explicit and conditionally stable. To consider the stability of the time evolution, we present the system of equations (18) in a modified recursive form

$$\begin{pmatrix} B^{n+\frac{1}{2}} \\ E^{n+1} \end{pmatrix} = \begin{pmatrix} I_{N_e} & -\Delta t \mathbf{d}_0 \\ \Delta t \star_\epsilon^{-1} \mathbf{d}_0^T \star_\nu & I_{N_v} - \Delta t^2 \star_\epsilon^{-1} \mathbf{d}_0^T \star_\nu \mathbf{d}_0 \end{pmatrix} \begin{pmatrix} B^{n-\frac{1}{2}} \\ E^n \end{pmatrix} + \begin{pmatrix} \Delta t & 0 \\ -\Delta t \star_\epsilon^{-1} \mathbf{d}_0^T \star_\nu & \Delta t \star_\epsilon^{-1} \end{pmatrix} \begin{pmatrix} J_H^n \\ J_E^{n+\frac{1}{2}} \end{pmatrix}, \quad n = 0, \dots, N-1, \tag{19}$$

where I_{N_e} on the upper left block of the coefficient matrix is an $N_e \times N_e$ identity matrix, whereas I_{N_v} on the lower right block of the coefficient matrix is an $N_v \times N_v$ identity matrix. By substituting, time step by time step, all the formulas of the earlier time steps to the formula with $n = N-1$, we find that the closed form representation to the solution, at the end of the considered time period, is

$$\begin{pmatrix} B^{N-\frac{1}{2}} \\ E^N \end{pmatrix} = \begin{pmatrix} I_{N_e} & -\Delta t \mathbf{d}_0 \\ \Delta t \star_\epsilon^{-1} \mathbf{d}_0^T \star_\nu & I_{N_v} - \Delta t^2 \star_\epsilon^{-1} \mathbf{d}_0^T \star_\nu \mathbf{d}_0 \end{pmatrix}^N \begin{pmatrix} B^{-\frac{1}{2}} \\ E^0 \end{pmatrix} \tag{20}$$

$$+ \sum_{k=0}^{N-1} \begin{pmatrix} I_{N_e} & -\Delta t \mathbf{d}_0 \\ \Delta t \star_\epsilon^{-1} \mathbf{d}_0^T \star_\nu & I_{N_v} - \Delta t^2 \star_\epsilon^{-1} \mathbf{d}_0^T \star_\nu \mathbf{d}_0 \end{pmatrix}^k \begin{pmatrix} \Delta t & 0 \\ -\Delta t \star_\epsilon^{-1} \mathbf{d}_0^T \star_\nu & \Delta t \star_\epsilon^{-1} \end{pmatrix} \begin{pmatrix} J_H^{N-1-k} \\ J_E^{N-1-k+\frac{1}{2}} \end{pmatrix}. \tag{21}$$

By assuming $J_H^n = J_E^{n+\frac{1}{2}} = 0 \ \forall \ n$, we have $u^N = G^N u^0$, where

$$u^N = \begin{pmatrix} B^{N-\frac{1}{2}} \\ E^N \end{pmatrix}, \quad G = \begin{pmatrix} I_{N_e} & -\Delta t \mathbf{d}_0 \\ \Delta t \star_\epsilon^{-1} \mathbf{d}_0^T \star_\nu & I_{N_v} - \Delta t^2 \star_\epsilon^{-1} \mathbf{d}_0^T \star_\nu \mathbf{d}_0 \end{pmatrix}, \quad u^0 = \begin{pmatrix} B^{-\frac{1}{2}} \\ E^0 \end{pmatrix}. \tag{22}$$

For a conditionally stable scheme, we need to find such choices of parameters that the numerical solution remains bounded. A necessary condition for stability is that the absolute values of the all eigenvalues of G must be less or equal to one and G must have a complete set of distinct eigenvalues and eigenvectors.[30] Instead of the eigenvalues λ for the matrix G we search for eigenvalues $\hat{\lambda} = \lambda - 1$ for matrix $\hat{G} = G - I_{(N_e+N_v)}$. We consider the eigenvalue equation $\hat{G}u = \hat{\lambda}u$, where u is the eigenvector, multiply the first row from left by $\star_\varepsilon^{-1}\mathbf{d}_0^T\star_\nu$ and solve it with respect to the first component of u, and substitute the result to the second row of the equation to get the characteristic equation

$$\hat{\lambda}^2 + \Delta t^2 \star_\varepsilon^{-1}\mathbf{d}_0^T \star_\nu \mathbf{d}_0\hat{\lambda} + \Delta t^2\star_\varepsilon^{-1}\mathbf{d}_0^T \star_\nu \mathbf{d}_0 = 0. \tag{23}$$

Since $\star_\varepsilon^{-1}\mathbf{d}_0^T \star_\nu \mathbf{d}_0$ is a diagonalizable matrix, multiplying it from right by the matrix of eigenvectors P and from left by the inverse of the matrix of eigenvectors P^{-1} results to the diagonal matrix with the eigenvalues of $\star_\varepsilon^{-1}\mathbf{d}_0^T \star_\nu \mathbf{d}_0$. Consequently, by multiplying Equation (23) from right by P and from left by P^{-1} results to the characteristic equation

$$\hat{\lambda}^2 + \Delta t^2\eta\hat{\lambda} + \Delta t^2\eta = 0, \tag{24}$$

where η are the eigenvalues of $\star_\varepsilon^{-1}\mathbf{d}_0^T \star_\nu \mathbf{d}_0$. Thus, the eigenvalues for G are

$$\lambda = \hat{\lambda} + 1 = 1 - 2\left(\left(\frac{\Delta t^2\eta}{4}\right) \pm \sqrt{\left(\frac{\Delta t^2\eta}{4}\right)^2 - \frac{\Delta t^2\eta}{4}}\right). \tag{25}$$

If $\frac{\Delta t^2\eta}{4} > 1$,

$$1 - 2\left(\left(\frac{\Delta t^2\eta}{4}\right) + \sqrt{\left(\frac{\Delta t^2\eta}{4}\right)^2 - \frac{\Delta t^2\eta}{4}}\right) < -1, \tag{26}$$

and the largest absolute value of the eigenvalues is larger than one. For $\frac{\Delta t^2\eta}{4} = 1$, there exists nondistinct eigenvalues $\lambda = 1 - \Delta t^2\eta/2$ and the stability is not satisfied. Thus, a necessary stability condition is $\Delta t^2\eta/4 < 1$, that is, $\Delta t < 2/\sqrt{\eta}$. In the case of square primal mesh elements, presented as an example in Figure 2, symbolic formulas for the eigenvalues η are obtained by an eigenvalue algorithm for heptadiagonal matrices.[31]

3.3 | Computational domain and boundary conditions

PCs are periodically structured electromagnetic media. In certain cases, PCs may exhibit photonic band gaps (PBG), which are ranges of frequency in which light cannot propagate through the structure. To consider the phenomenon, we model a 2D square symmetrical PC, constructed of the cross-section of dielectric rods in the air substrate, in a rectangular domain illustrated in Figure 4. The radius of each dielectric rod is r and the lattice constant $a = 1$ is the distance between the centers of two nearest dielectric rods. Due to symmetry, we can restrict ourselves to simulate a rectangular domain $[0, 10] \times [0, 1]$, that is, a single row of the crystal, and terminate the upper and lower boundary with a perfect magnetic conductor (PMC) or periodic boundary condition.

The update formulas (18) naturally implement a PMC boundary.[2] To enforce the periodic boundary condition we could use a cylindrical shape of the domain and a mesh with a suitable metric to derive the discrete Hodge star operators. However, here we get to the same result by modifying the update formulas derived for the rectangular domain. The computational domain is discretized, also with a triangular primal mesh, such that each point on the lower boundary corresponds to a point on the upper boundary with the same x_1-coordinate. Let σ be a map relating the indices of the bottom vertices to the corresponding indices on the top vertices. Using a projection matrix of the form

$$P_{i;i} = P_{j;\sigma(j)} = P_{\sigma(j);j} = 1 \text{ for all top vertices } v_i \text{ and bottom vertices } v_j,$$

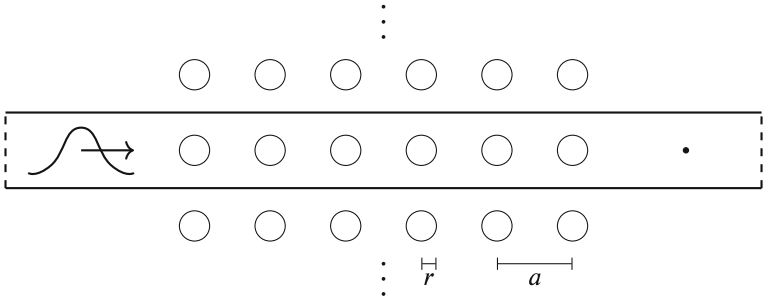

FIGURE 4 Illustration of the simulation setup, solid lines are joined together and dashed lines represent absorbing boundaries, the single dot on the right side is the reference point where electric field strength is recorded.

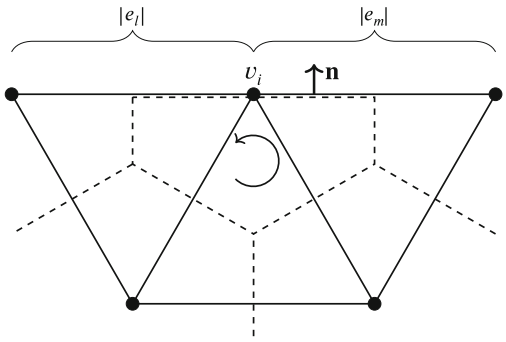

FIGURE 5 Completing the circulation around a boundary node v_i

we can join the values of the top and bottom vertices of the mesh. Also noting that on the cylindrical mesh the dual area of a point joined by the periodic boundary condition should be the sum of the dual areas of the joined points, we get the modification

$$\hat{\star}_{\epsilon\{j;j\}} = \hat{\star}_{\epsilon\{\sigma(j);\sigma(j)\}} = \star_{\epsilon\{j;j\}} + \star_{\epsilon\{\sigma(j);\sigma(j)\}}$$

for all bottom boundary vertices j.

The left- and right-hand sides of the computational domain are considered as absorbing boundaries. The absorbing boundary condition is implemented on the boundary of the domain as $J_E^{n+\frac{1}{2}} = \star_\partial E^n$ with

$$\star_{\partial ii} = -\sqrt{\frac{\varepsilon}{\mu}}\frac{1}{2}\left(|e_l| + |e_m|\right), \tag{27}$$

where i is the index of a boundary vertex and $|e_l| + |e_m|$ is the sum of the lengths of the boundary edges linked to the ith boundary vertex v_i (see Figure 5). All the terms $\star_{\partial ii}$ have the same sign because the simplices have the same orientation.

4 | NUMERICAL RESULTS

In this section, we present numerical tests on transmission conditions, material properties, geometry approximation, mesh refinements strategies, and band gaps of PCs and compare the triangular DEC discretization with the square element based FDTD discretization. We have used the DEC code implemented in C++ at the University of Jyväskylä.[15] In principle, the solver is based on generalized finite differences, covering as a special case also the FDTD method. That is, it is possible to compare the DEC discretization with a computational mesh with triangular face elements with the FDTD as a special case constructed with a computational mesh with rectangular face elements. However, we used for the FDTD tests a program implemented in Matlab by the second author.

For all the simulations we set $\mu = 1.0$ and modeled the material properties by varying the values of ε. The time domain simulations are initialized at $t = 0$ and finished at $t = 200$. With the FDTD we have used time step length $\Delta t = 9h/10\sqrt{2}$ and with the DEC $\Delta t = h_{\max}/4$, where $h_{\max}$ is the largest edge length of the primal mesh. This implies that in the FDTD discretizations $\Delta t/h \approx 0.64$ and in the DEC discretizations $\Delta t/h_{\min}$ varies between 0.55 and 0.88 and the stability criteria are satisfied. The band structure graphs are obtained as eigenvalue problem solutions in frequency domain by following Chen and Chew.[2] We start with naive examples to demonstrate the simulation challenges and proceed to conquer them by adjusting material properties and optimizing and refining the mesh.

4.1 | Transmission

Here we examine a method for finding the transmission coefficients for different wavelengths of TM-polarized light through a 2D square symmetrical PC. We send a incident wave from all of the left side boundary vertices by adding to their values at time instance t the modified Gaussian function

$$g(t) = e^{-((t-t_0)/d)^2} \sin(2\pi f_m(t - t_0)), \tag{28}$$

where $d = 3/\pi f_m$ defines the half-bandwidth of the pulse and f_m is the center of the frequency area of interest.[32] The wavelength λ inside the surrounding medium is one half of the lattice constant a. Furthermore, the time shift $t_0 = 3d$ reduces the effect of the initial discontinuity when the source is turned on at $t = 0$. Equation (28) is discretized as $g^n = g(n\Delta t)$, leading to an additional update formula

$$E^n|_{\text{lhs}} = E^n|_{\text{lhs}} + g^n$$

on the left-hand side boundary vertices.[33]

The transmission coefficient is computed by repeating the simulation twice, one simulation measuring transmitted waves with the dielectric rods and one as incident wave in the homogeneous domain without dielectric rods.[34] During the simulations, we obtain in time domain the field histories at a reference point on the right-hand side of the most right-hand rod as E^n_{rods} and $E^n_{\text{no rods}}$, $n = 0, \ldots, N-1$, respectively. Further, the time domain values are transformed to the frequency domain values $E_{\text{rods}}(\omega)$ and $E_{\text{no rods}}(\omega)$, respectively, with the discrete Fourier transform to get the transmission coefficient in decibels for frequency ω as

$$20 \cdot \log_{10}\left(\frac{|E_{\text{rods}}(\omega)|}{|E_{\text{no rods}}(\omega)|}\right). \tag{29}$$

In the first example, we discretize the computational domain by a triangle mesh with 10 edges (11 mesh points) per unit length on the boundary (see Figure 6). We set $\lambda = 1$, radius of each dielectric rod $r = 0.3\lambda$, and permittivity of rods $\varepsilon^{\max} = 5.9$, while for air $\varepsilon = 1.0$. Simulating the setup with $f_m = 0.45$, $d = 6a/\pi$ and $\omega = 6/\pi$ leads to graphs presented in Figure 7 showing clear gaps in the transmission coefficient around frequencies 0.3 and 0.6.

The results presented in Figure 8 are in good agreement with the band structure considerations presented by Chen and Chew.[2] However, in our simulations, the PBG seems to extend below the frequency 0.3 unlike in the band structure diagram. This is likely because these modes in the band structure diagram correspond to diagonally traveling waves which our simulations do not address. Modeling of the circular cross-sections of the rods together with the coarseness of the mesh is a source of inaccuracies.

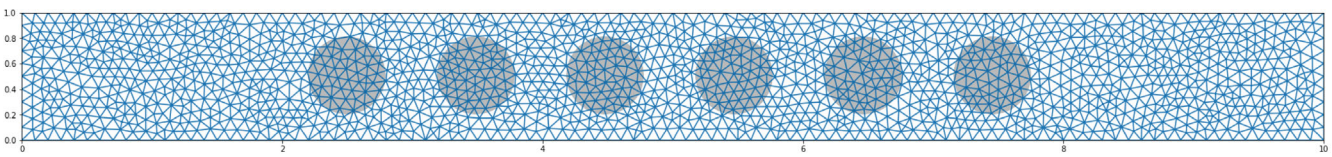

FIGURE 6 Computational domain and primal mesh with 10 edges (11 mesh points) per unit length on the boundary. The cross-sections of the rods are colored in gray.

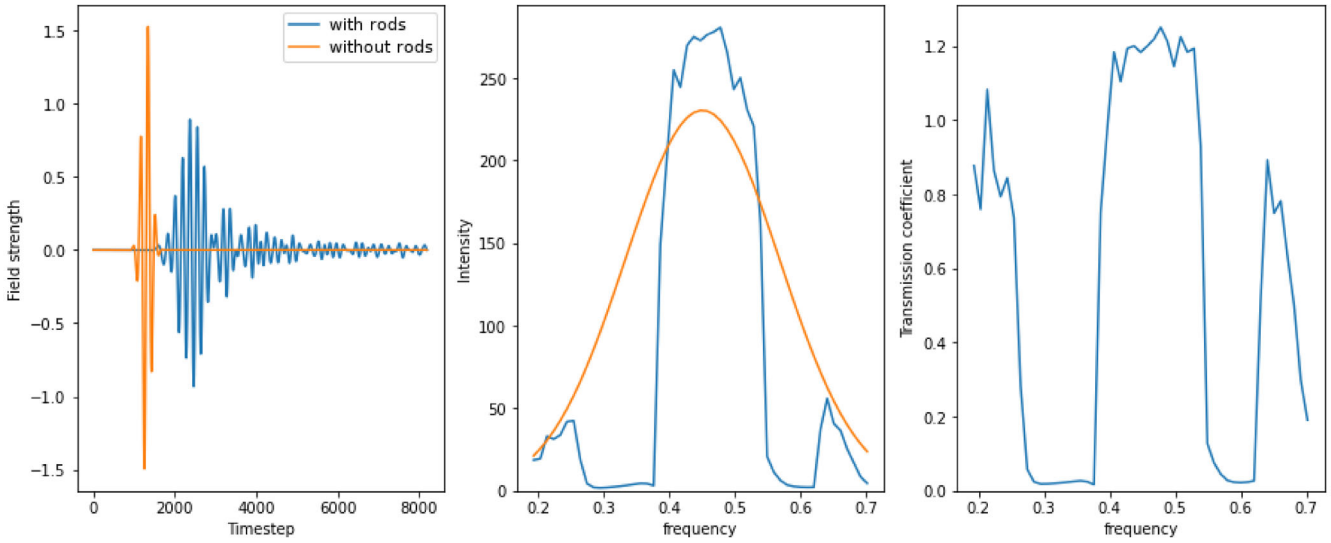

FIGURE 7 Simulation results for $r = 0.3$ and $\epsilon^{\max} = 5.9$

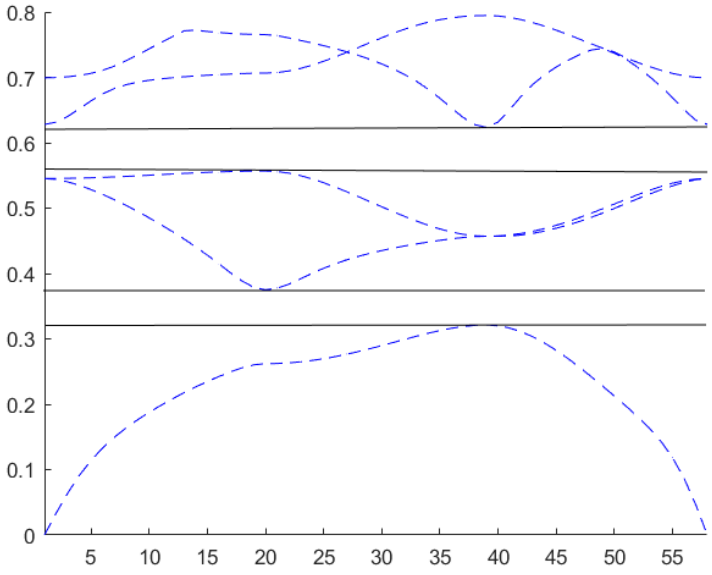

FIGURE 8 Band structure of PC with $r = 0.3$ and $\epsilon^{\max} = 5.9$

4.2 | Adjusted material and geometry approximation for the dielectric rods

Since geometric modeling of the circular cross-sections of the rods is an important source of error, we observe this error source by numerical tests and propose remedies by adjusting both the mesh and the material properties. With both the conventional FDTD and the DEC it is common to model the rods or other inhomogeneities by adjusting the permittivity of a mesh point based on whether the point is within the radius of the cross-section of the rod or not. We tested how a strict rectangular approximation limits the choice of mesh resolution, that is, the number of mesh points per unit length, by setting the radius of cross-sections of the rods $r = 0.2$ and electric permittivity of the rods $\epsilon^{\max} = 8.9$ and using several mesh resolutions. The effective area of the cross-section of the dielectric rod was set as

$$A_{\text{eff}} = \sum_i \frac{\varepsilon_i - 1}{\epsilon^{\max} - 1} |\Omega_i^*|,$$

where the sum goes over all the vertices inside a periodic cell, ϵ_i is the permittivity assigned to the vertex i, and $|\Omega_i^*|$ is the area of the dual face of the vertex i. Effective radius r_{eff} is the radius of a circle with an area of A_{eff}. The wave field strength is measured at reference point $(9.0, 0.5)$.

In Figure 9, we see that effective radius $r_{\text{eff}} = 0.2$ provides the transmission curve (left bottom figure) without significant loss of accuracy for all tested mesh resolutions of 22, 32, 34, and 39 points per unit length (marked by red stars in the top figure). The deviation in the effective radius of the cross-section of the rod is shown to decrease the accuracy of the transmission simulation, as is presented for the mesh resolutions of 29, 33, 37, and 40 points per unit length (marked by blue stars in the top figure) in the right bottom figure in Figure 9. Thus, for the FDTD, that is, rectangular face elements, the geometry approximation of the rods is poor, unless a very fine mesh is used, and can be significantly improved by scaling the permittivity of a point based on how much of the corresponding dual area is inside the circle.

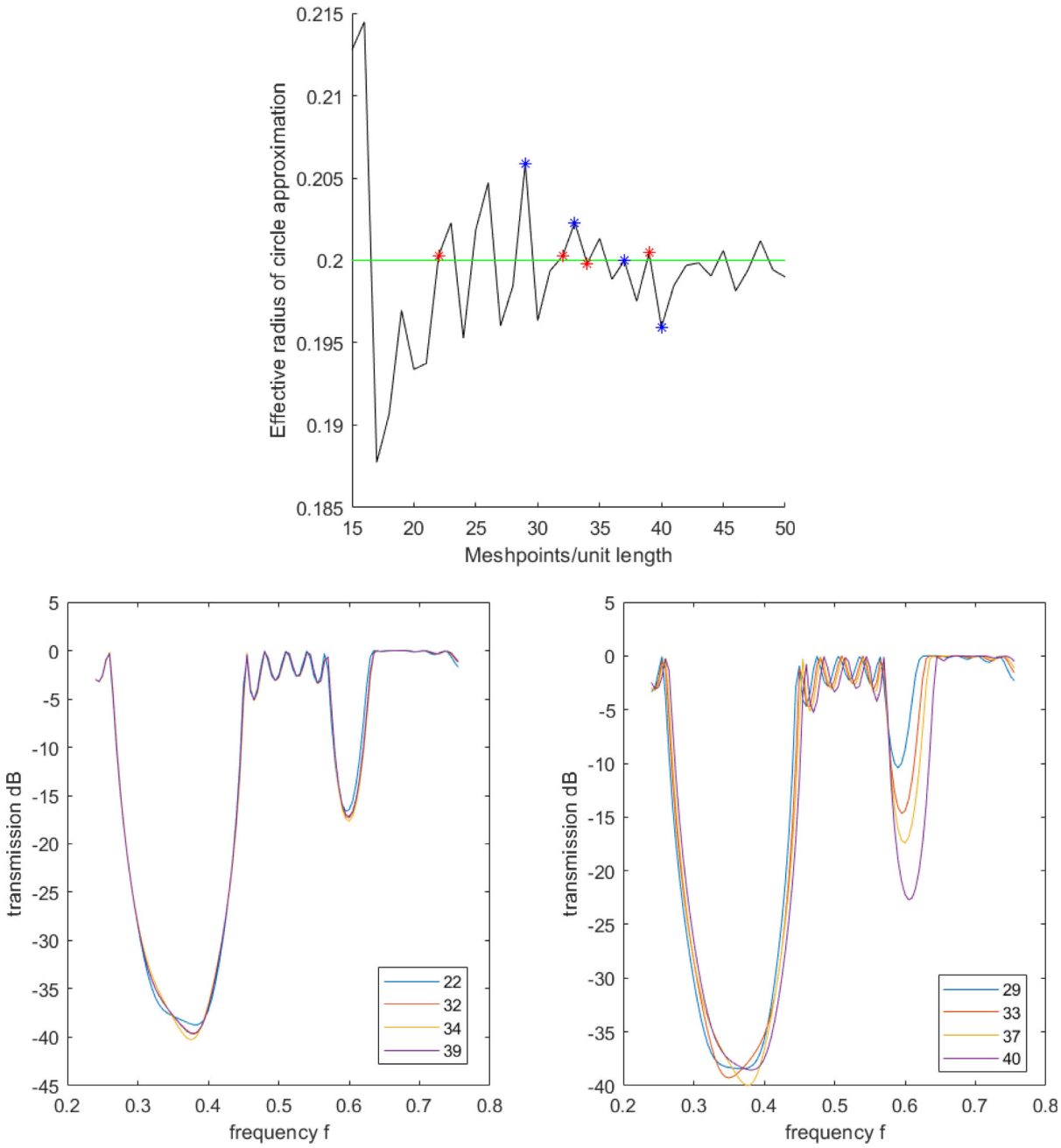

FIGURE 9 Approximating the circular cross-sections of a dielectric rod with rectangles, the accuracy of the approximation and simulation results depend strongly on the number of mesh points per unit length.

In Figure 10, we demonstrate the effect of scaling the permittivity. The horizontal axis represents the modeling accuracy used to calculate the scaled permittivity for points near the boundary of a rod, and the value 1 corresponds to no scaling. The accuracy of the solution (red line in Figure 10) is directly related to the difference in effective radius (blue line in Figure 10) when the difference between radiuses is greater than 0.001. The radius of cross-sections of the rods was $r = 0.2$, so this corresponds to an error of 0.5%. For values smaller than this, it is likely still an important factor.

With the DEC, utilizing also triangular elements, we can model the mesh so that it approximates the cross-section of a dielectric rod more accurately. First we model the rod with a regular n-gon so that the effective area is exactly equal to the area of the rod cross-section. Since the edges of the n-gon need to be edges of the dual mesh, we draw appropriate sized circles to the n-gon vertices and construct tetragons based on the intersection points of these circles. The remaining areas are filled with a triangular mesh. The resulting mesh, for a low level discretization, of 11 points per unit length on the boundary is illustrated in Figure 11. In what follows, we call the mesh obtained by this construction as optimal or optimized mesh. This method can be straightforwardly generalized to accurately model arbitrary shaped material boundaries.

We consider the accuracy of the space discretization methods by comparing the transmission graphs, and measure the difference between the methods X and Y as the root mean square deviation (RMSD) calculated as

$$\mathrm{RMSD}(X, Y, F) = \frac{\sqrt{\sum_{f \in F} (x_f - y_f)^2}}{\sqrt{|F|}},$$

where the sum goes over all the discrete frequencies of interest F, x_f and y_f are the transmissions in decibels corresponding to the frequency f, obtained by methods X and Y, respectively, and $|F|$ is the number of discrete frequencies. The compared models are the FDTD with no permittivity scaling, the FDTD with permittivity scaling, and the DEC with an optimized mesh. Each of the compared simulations is setup so that they have exactly the same effective radius. For the first comparison we use the radius of the dielectric rod $r = 0.2$, electric permittivity $\varepsilon^{\max} = 8.9$, and 36 mesh points per unit length on the boundary. For the second comparison $r = 0.3$, $\varepsilon^{\max} = 5.9$, and there were 31 mesh points per unit length on the boundary. The frequency-transmission graphs through 6 layers and comparison between the models are shown in Figures 12 and 13, where the difference between the compared solutions is presented as a black graph, the transmission of the first mentioned method as a blue graph and the last mentioned method as a red graph. The deviation seems to be

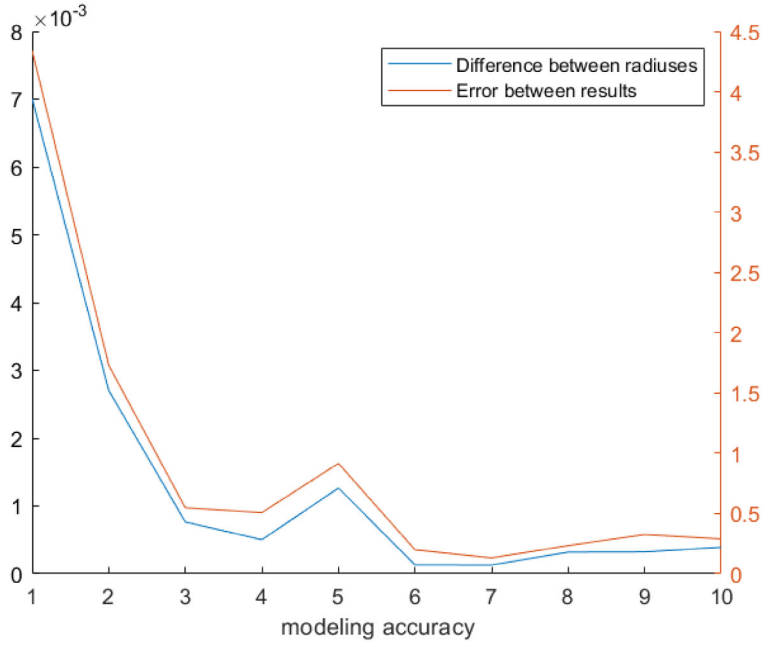

FIGURE 10 Difference between transmission graphs compared to the difference between the effective radius of the cross-sections of dielectric rods. The compared simulations used a discretization of 23 and 24 mesh points per unit length.

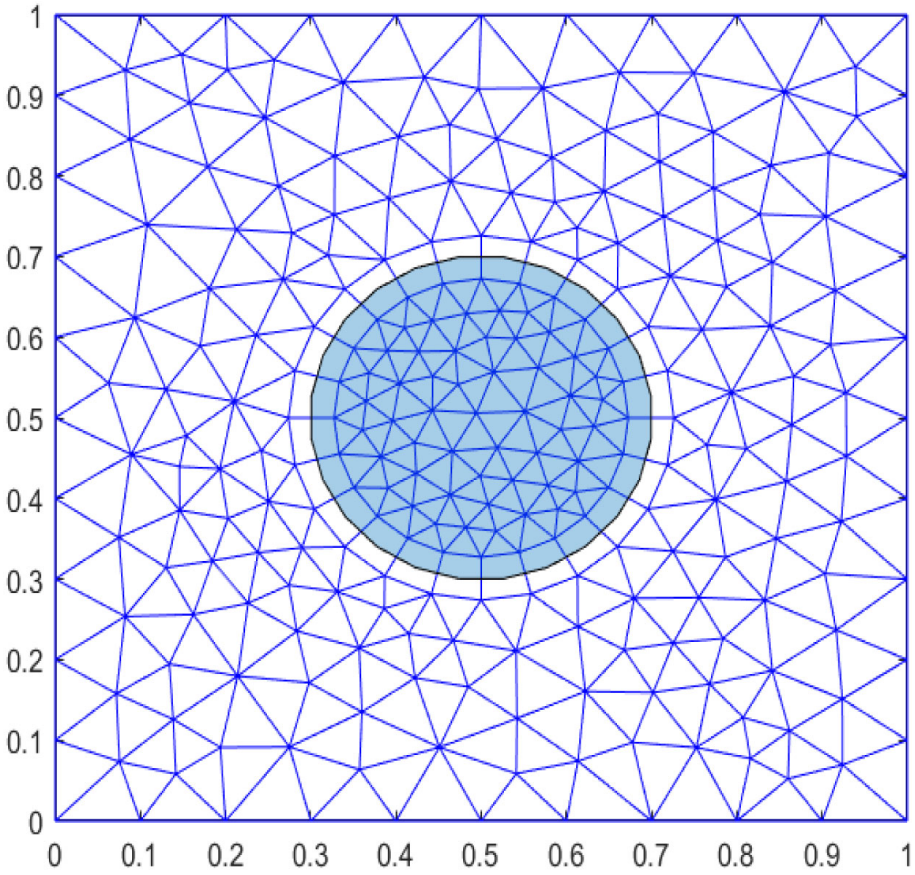

FIGURE 11 A mesh optimized for modeling the geometry of the rod. The colored area is the union of all the dual faces of vertices within the rod.

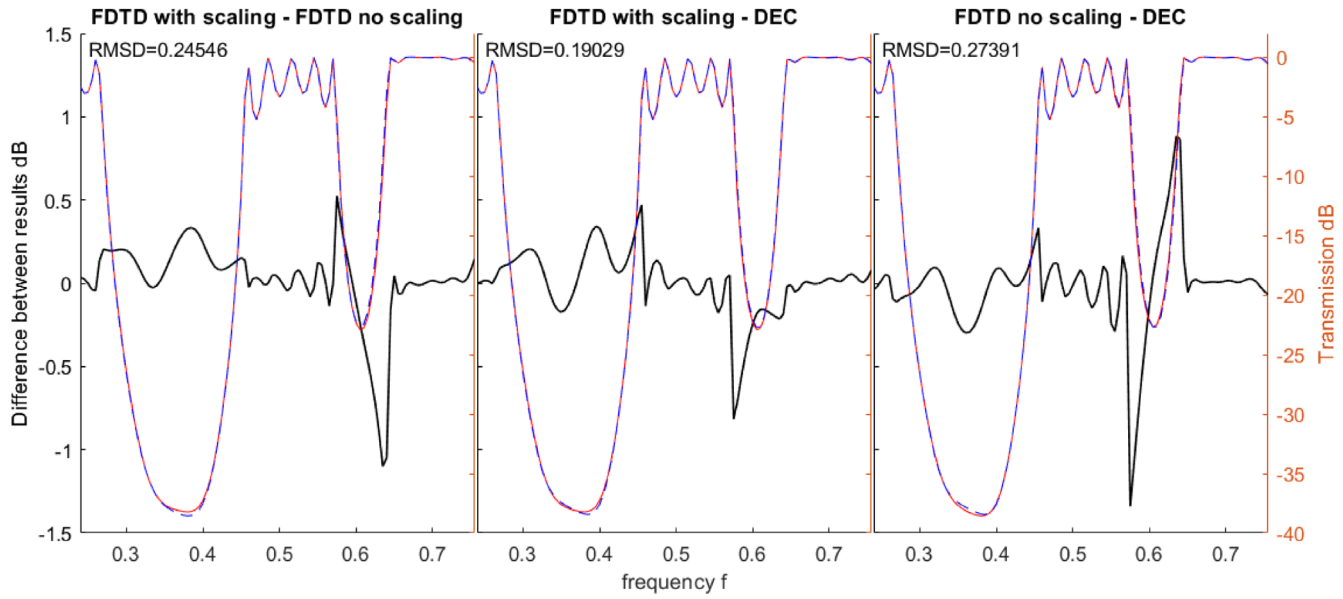

FIGURE 12 Difference and root mean square deviation between the different methods for $r = 0.2$, $\epsilon^{\max} = 8.9$, and 36 mesh points per unit length on the boundary

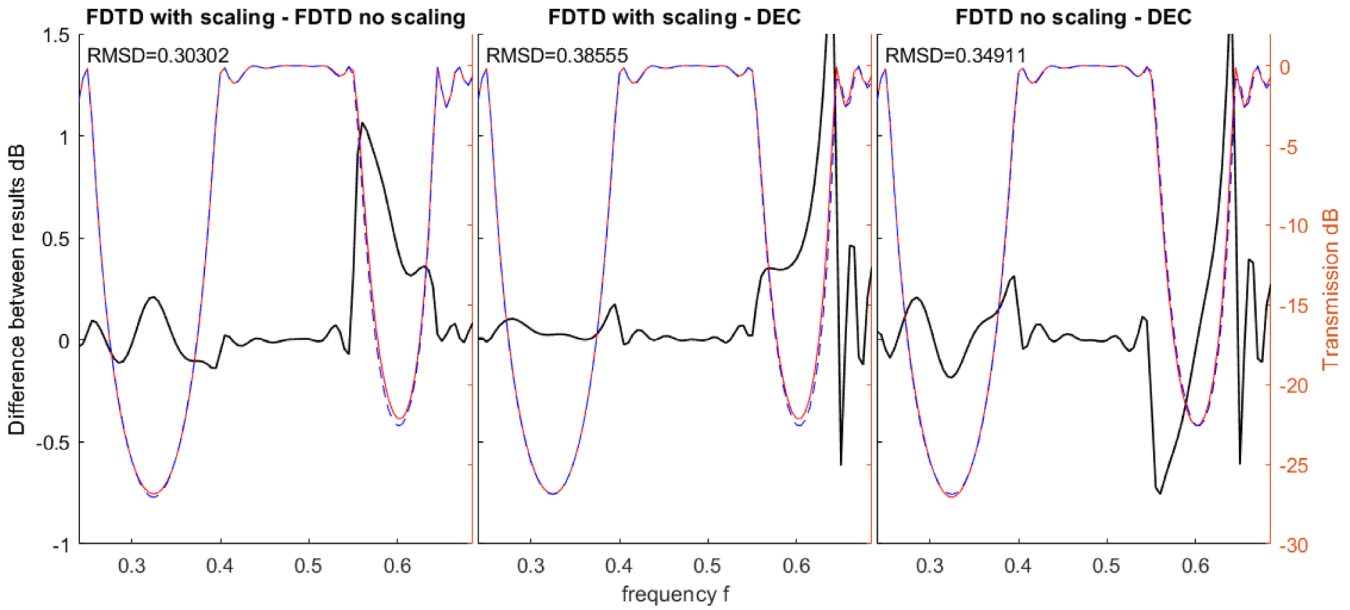

FIGURE 13 Difference and root mean square deviation between the different methods for $r = 0.3$, $\varepsilon^{\max} = 5.9$, 31 mesh points per unit length on the boundary

largest in areas where there is a sudden change in transmission. This is natural since these are also the most challenging parts to model accurately. The deviation seems to also increase with frequency, which is likely due to the decreasing wavelength and consecutively the number of mesh points per wavelength getting smaller. Some of the spikes in the error graphs could also be attributed to a slight frequency shift. The increase in the edge length, or mesh stepsize, raised all of the RMSDs as could be expected. In all the test cases, the obtained transmission graph was qualitatively valid. Permittivity scaling and mesh optimization have the benefit that they can be applied with high accuracy to any radius and discretization.

4.3 | Mesh refinement

We study numerically the convergence rate and accuracy of the FDTD with parameter scaling and the DEC with an optimal mesh. The FDTD setup is truncated with a CFS-PML absorbing boundary layer[27] on the left and right side of the computational domain. The top and bottom sides are joined to effectively make the simulation area a cylinder. For the first test case, we study transmission through 6 layers, $r = 0.2$, and $\varepsilon^{\max} = 8.9$. The reference solution is calculated by linear extrapolation of three FDTD simulations using discretizations of 80, 90, and 100 points per unit length. The error for each simulation result is calculated as the RMSD to this reference solution. The results shown in Figure 14 show clear convergence in terms of mesh edge length. For the DEC, we have reported both the largest edge length (red stars in Figure 14, "DEC max dx") and the smallest edge length (black stars in Figure 14, "DEC min dx"). The convergence of the DEC in terms of the largest edge length has the same trend as the convergence of the FDTD (blue stars in Figure 14). Thus, the maximum edge length is the limiting factor for the accuracy and the use of a mesh that optimizes the material boundary modeling gains no significant improvement in the overall accuracy with this choice of parameters, geometry, and mesh refinement. Repeating the experiment for $r = 0.3$ and $\varepsilon^{\max} = 5.9$ shows (see Figure 15) a slight increase in accuracy for the DEC. By comparing the transmission graphs in Figures 12 and 13, we also observe that the transmission graph with this test's parameters is a bit smoother in the sense that it has gentler slopes.

As earlier mentioned, the error is related to the rate of change in the transmission graph and increases with frequency. Both of the methods tended to overestimate transmission in places where the slope of the transmission graph is positive and underestimate if the slope was negative, which could be the result of a slight frequency shift. This is demonstrated in Figure 16. Based on the above mentioned observations, we choose three points (marked as black stars

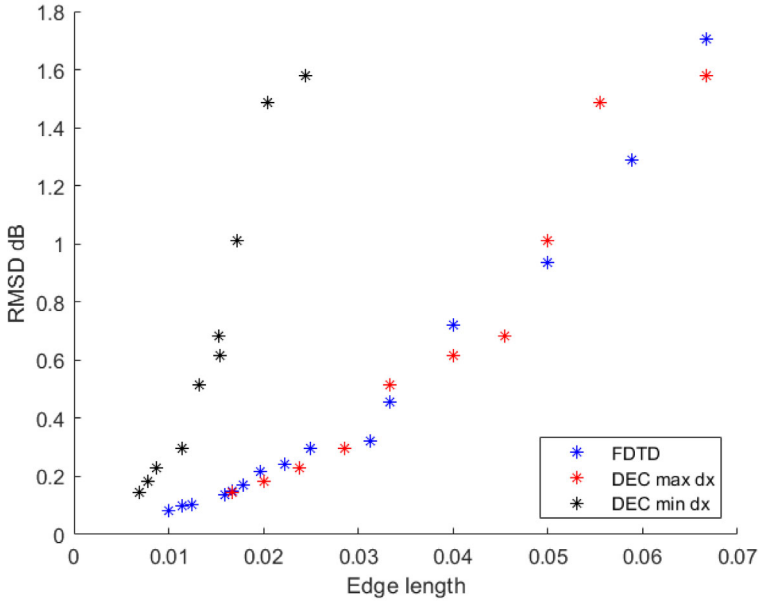

FIGURE 14 RMSD to the reference solution for different levels of discretization ($r = 0.2$ and $\epsilon^{\max} = 8.9$)

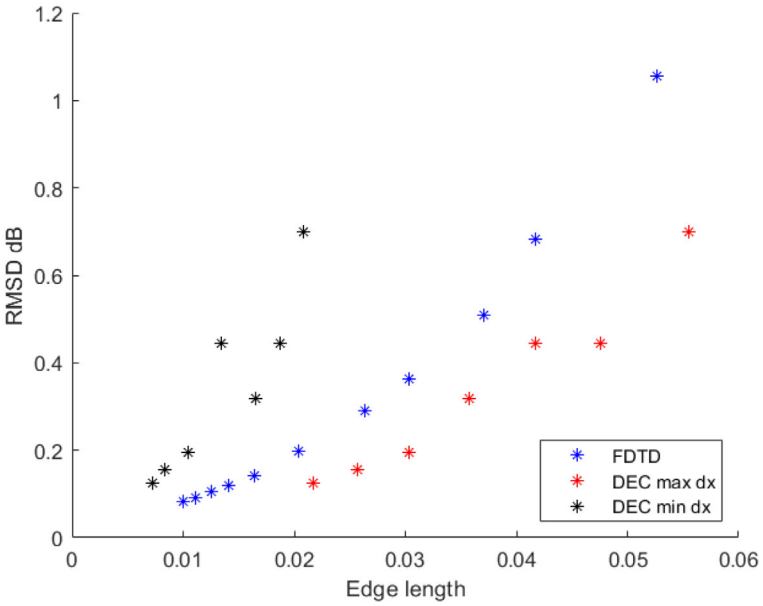

FIGURE 15 RMSD to the reference solution for different levels of discretization ($r = 0.3$ and $\epsilon^{\max} = 5.9$)

in the top figure in Figure 16) in the transmission graph and take a closer look of the transmission with respect to the edge length. In the bottom figure in Figure 16, we present the results with the FDTD with scaling (blue stars) and the DEC in terms of the largest edge length (red stars) and the reference solution (black star) for each of the chosen frequencies.

Since the compared methods had different boundary conditions (Silver–Müller and PMC for DEC, CFS-PML and periodic for FDTD) we should investigate if the choice of boundary condition has an affect on the results. Using the same rectangular mesh for both methods and measuring the RMSD of the transmission graphs, we get the results presented in Figure 17. Comparing this to Figure 14 or Figure 15, we conclude that the deviation is nearly an order of magnitude smaller and conclude that the use of different boundary conditions is not a significant error factor in the comparisons presented above.

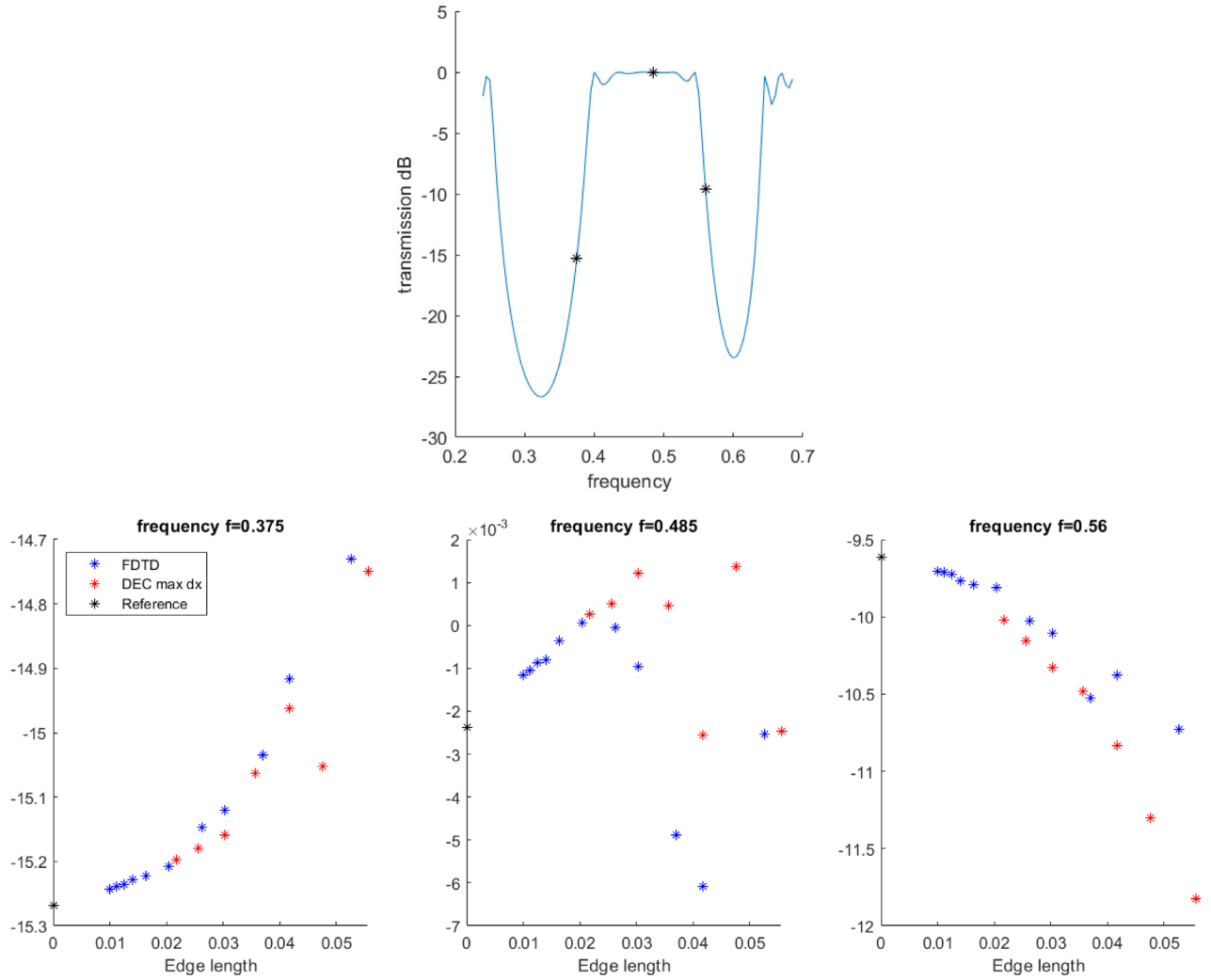

FIGURE 16 Transmission for different frequencies and discretizations

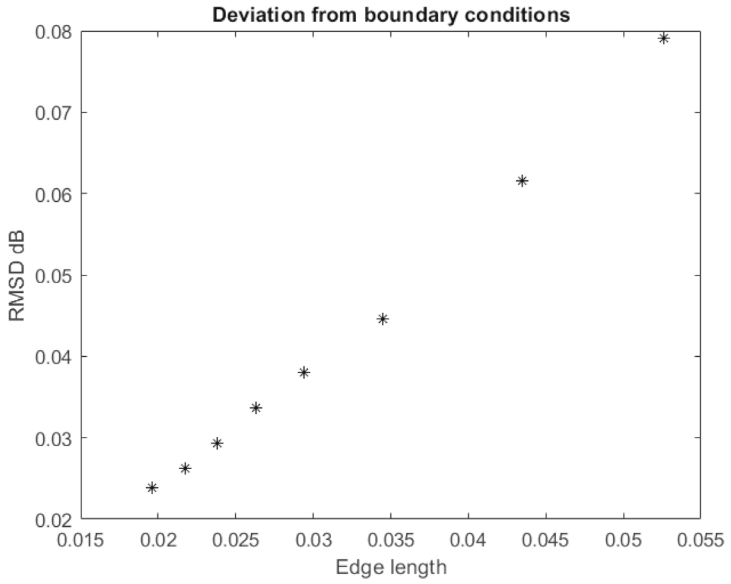

FIGURE 17 The difference between the boundary conditions

4.4 | Photonic band gap

A photonic band gap is a range of frequencies in which there does not exist propagating waves for any wavenumber, but there are propagating waves above and below the band gap. To find the band gap frequencies we compute, for $r = 0.2$, band structure graphs with two different permittivities. We present the graphs along the points G, X, and M (see Figure 18) of the Brillouin zone[35] for the TM modes. We are considering a normally incident wave, and thus we can concentrate on the section $[G, X]$ of the band structure. In Figures 19 and 20, we illustrate the band structures, side-by-side with the transmission graphs, with $\epsilon^{\max} = 8.9$ and $\epsilon^{\max} = 5.9$, respectively. We observe two band gaps bounded by the blue dashed lines in both figures. The photonic band gaps are clearly positioned in the frequencies related to the pits in the transmission graphs. By introducing a line defect to the PC, frequencies within the bandgap are strongly confined inside the line defect.

In the last numerical tests, we use the DEC space discretization with $r = 0.2$, $\epsilon^{\max} = 8.9$, $h_{\max} = 1/32$, and $h_{\min} \approx 0.4h_{\max}$ in an area of 15×7 periodic cells with the rods in the middle row removed. We set a narrow width modified Gaussian pulse, first centered around the frequency 0.4 and in another test run centered around the frequency 0.5, as a source in the middle of the left-hand side boundary and simulate with respect to time with $\Delta t \approx 0.008$. As expected from the band structure and transmission graph 19, only the pulse corresponding to the frequency 0.4 is confined within the line defect (see Figure 21).

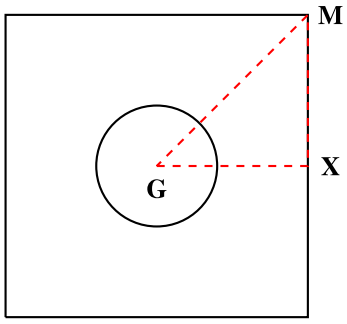

FIGURE 18 The band structure is calculated by solving an eigenvalue problem at the points of the irreducible Brillouin zone highlighted in red

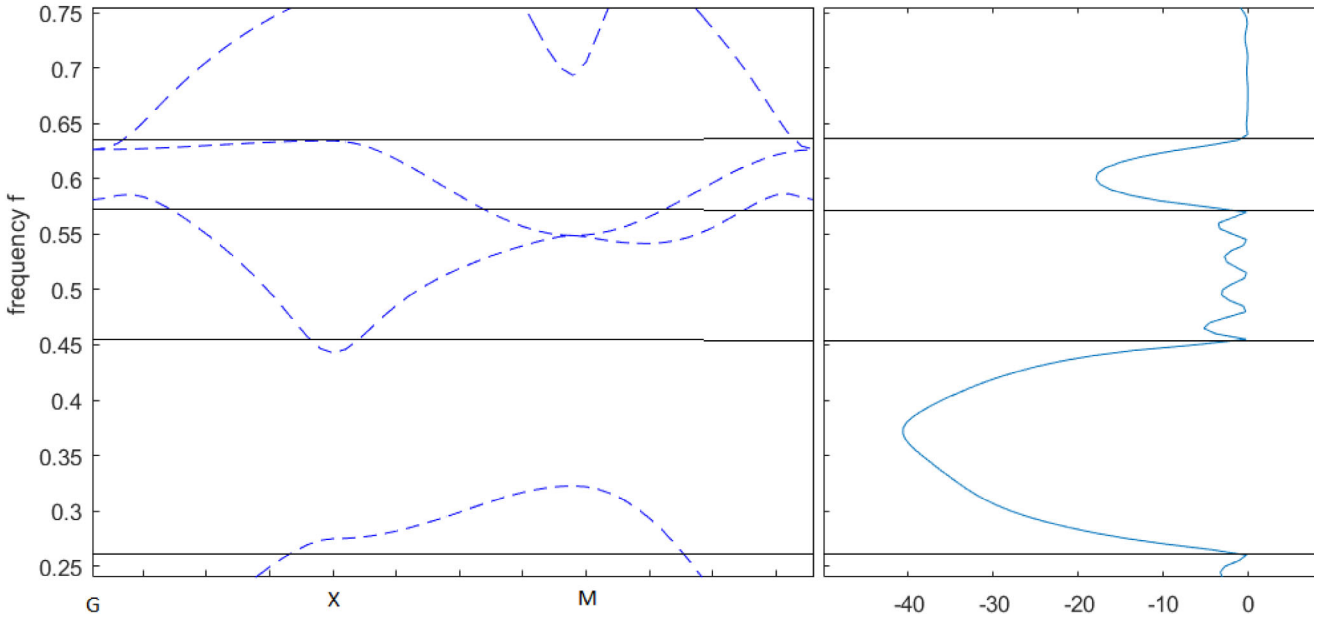

FIGURE 19 Comparison of the band structure and transmission graphs for $r = 0.2$, $\epsilon^{\max} = 8.9$

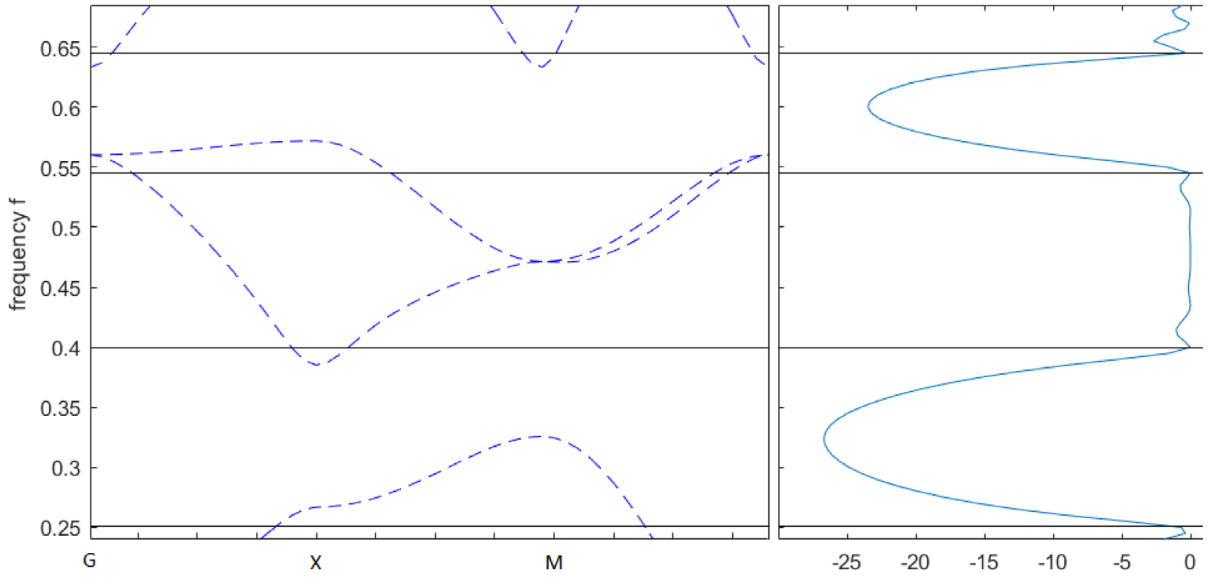

FIGURE 20 Comparison of the band structure and transmission graphs $r = 0.3$, $\epsilon^{\max} = 5.9$

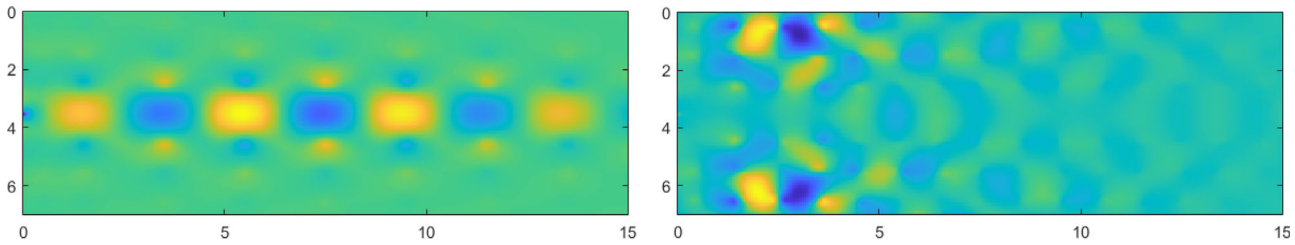

FIGURE 21 Pulses centered around frequencies 0.4 (left) and 0.5 (right) in a photonic crystal array

5 | CONCLUSIONS

We presented two-dimensional DEC discretization for PCs and demonstrated it with numerical experiments on material properties, geometry approximation, and mesh refinement strategies and demonstrated how the band gap frequencies are related to the transmission conditions. Modeling the circular cross-sections of the dielectric rods accurately and running the simulations computationally efficiently is a challenging task especially if only rectangular mesh elements can be used. However, the accuracy can be increased by scaling the permittivity on the rod boundary and adjusting the radius to better match the area. With the DEC, utilizing more generalized or mixed types of polygonal elements, there is also the option of designing the mesh to better match the nonpolygonal material boundaries. Hence, the DEC is well-suited for PC waveguide problems and with the diagonal discrete Hodge star operator it is computationally efficient especially in time-domain simulations.

ACKNOWLEDGMENTS

The authors would like to thank Jukka Räbinä for the discrete exterior calculus implementation and Tytti Saksa for discussions on discrete schemes.

DATA AVAILABILITY STATEMENT

The data that support the findings of this study are available from the corresponding author upon reasonable request.

ORCID

Sanna Mönkölä https://orcid.org/0000-0001-5843-2533

REFERENCES

1. Ikuno H, Naka Y. Finite-difference time-domain method applied to photonic crystals. In: Yasumoto H, ed. *Electromagnetic Theory and Applications for Photonic Crystals*. CRC Press; 2018:401-444.
2. Chen SC, Chew WC. Numerical electromagnetic frequency domain analysis with discrete exterior calculus. *J Comput Phys*. 2017;350:668-689.
3. Jyothish M, Francis F, Manivasakan R. Finite element method (FEM) computations in frequency domain & photonic band diagram: applications to microcavity characterization. *Optik*. 2021;245:167614.
4. Askarian A. Design and analysis of all optical half subtractor in 2D photonic crystal platform. *Optik*. 2021;228:166126.
5. Haider MA, Venakides S, Papanicolaou V. Boundary integral calculations of two-dimensional electromagnetic scattering by photonic crystal Fabry–Perot structures. *SIAM J Appl Math*. 2000;60(5):1686-1706.
6. Jerez-Hanckes C, Durán M, Guarini M. Hybrid FEM/BEM modeling of finite-sized photonic crystals for semiconductor laser beams. *Int J Numer Methods Eng*. 2010;82(10):1308-1340. doi:10.1002/nme.2803
7. Rodríguez-Esquerre VF, Koshiba M, Hernández-Figueroa HE. Finite-element analysis of photonic crystal cavities: time and frequency domains. *J Lightwave Technol*. 2005;23(3):1514.
8. Zhang T, Sun J, Yang Y, Li Z. Photonic crystal filter based on defect mode and waveguide mode symmetry matching. *Opt Commun*. 2018;428:53-56.
9. Zhu B, Chen J, Zhong W, Liu QH. Analysis of photonic crystals using the hybrid finite-element/finite-difference time domain technique based on the discontinuous Galerkin method. *Int J Numer Methods Eng*. 2012;92(5):495-506. doi:10.1002/nme.4348
10. Räbinä J, Kettunen L, Mönkölä S, Rossi T. Generalized wave propagation problems and discrete exterior calculus. *ESAIM Math Model Numer Anal*. 2018;52(3):1195-1218. doi:10.1051/m2an/2018017
11. Bossavit A, Kettunen L. Yee-like schemes on a tetrahedral mesh, with diagonal lumping. *Int J Numer Model Electron Netw Dev Fields*. 1999;12(1-2):129-142.
12. Desbrun M, Hirani AN, Marsden JE. Discrete exterior calculus for variational problems in computer vision and graphics. Proceedings of the 42nd IEEE International Conference on Decision and Control (IEEE Cat. No. 03CH37475); 2003:4902-4907; IEEE.
13. Bell N, Hirani AN. PyDEC: software and algorithms for discretization of exterior calculus. *ACM Trans Math Softw (TOMS)*. 2012;39(1):1-41.
14. Boom PD, Kosmas O, Margetts L, Jivkov AP. A geometric formulation of linear elasticity based on discrete exterior calculus. *Int J Solids Struct*. 2022;236:111345.
15. Räbinä J, Mönkölä S, Rossi T. Efficient time integration of Maxwell's equations with generalized finite differences. *SIAM J Sci Comput*. 2015;37(6):B834-B854.
16. da Silva L, Batista C, González I, Macêdo A, de Oliveira W, Melo S. A discrete exterior calculus approach to quantum transport and quantum chaos on surface. *J Comput Theor Nanosci*. 2019;16(9):3670-3682.
17. Räbinä J, Kuopanportti P, Kivioja MI, Möttönen M, Rossi T. Three-dimensional splitting dynamics of giant vortices in Bose-Einstein condensates. *Phys Rev A*. 2018;98:023624. doi:10.1103/PhysRevA.98.023624
18. Nitschke I, Reuther S, Voigt A. Discrete exterior calculus (DEC) for the surface Navier-Stokes equation. In: Bothe D, Reusken A, eds. *Transport Processes at Fluidic Interfaces*. Springer; 2017:177-197.
19. Chen SC, Chew WC. Electromagnetic theory with discrete exterior calculus. *Prog Electromagn Res*. 2017;159:59-78.
20. Kettunen L, Lohi J, Räbinä J, Mönkölä S, Rossi T. Generalized finite difference schemes with higher order Whitney forms. *ESAIM Math Model Numer Anal*. 2021;55(4):1439-1459.
21. Toshniwal D, Hughes TJ. Isogeometric discrete differential forms: non-uniform degrees, Bézier extraction, polar splines and flows on surfaces. *Comput Methods Appl Mech Eng*. 2021;376:113576.
22. Lindqvist H, Martikainen J, Räbinä J, Penttilä A, Muinonen K. Ray optics for absorbing particles with application to ice crystals at near-infrared wavelengths. *J Quant Spectrosc Radiat Transf*. 2018;217:329-337.
23. Swarnakar S, Kumar S, Sharma S. Design of all-optical half-subtractor circuit device using 2-D principle of photonic crystal waveguides. *J Opt Commun*. 2019;40(3):195-203.
24. Elhachemi K, Rafah N. A novel proposal based on 2D linear resonant cavity photonic crystals for all-optical NOT, XOR and XNOR logic gates. *J Opt Commun*. 2020;000010151520200184.
25. Tang W, Chen C. Hydrogel-based colloidal photonic crystal devices for glucose sensing. *Polymers*. 2020;12(3):625.
26. Liu W, Ma H, Walsh A. Advance in photonic crystal solar cells. *Renew Sust Energ Rev*. 2019;116:109436.
27. Moura AS, Saldanha RR, Silva EJ, Pantoja MF, Lisboa AC, Facco WG. Discretization of the CFS-PML for computational electromagnetics using discrete differential forms. *Microw Opt Technol Lett*. 2013;55(2):351-357.
28. Radożycki T. Reduction of the classical electromagnetism to a two-dimensional curved surface. *J Mod Opt*. 2019;66(9):1029-1037.
29. Desbrun M, Kanso E, Tong Y. Discrete differential forms for computational modeling. In: Bobenko AI, Schröder P, Sullivan JM, Ziegler GM, eds. *Discrete Differential Geometry*. Springer; 2008:287-324.
30. Gedney SD, Roden JA. Numerical stability of nonorthogonal FDTD methods. *IEEE Trans Antennas Propag*. 2000;48(2):231-239.

31. Lita da Silva J. On the characteristic polynomial, eigenvectors and determinant of heptadiagonal matrices. *Linear Multilinear Algebra*. 2017;65(9):1852-1866.
32. Danaie M, Geravand A, Mohammadi S. Photonic crystal double-coupled cavity waveguides and their application in design of slow-light delay lines. *Photon Nanostruct Fund Appl*. 2018;28:61-69.
33. Taflove A, Hagness SC. *Computational Electrodynamics: The Finite-Difference Time-Domain Method*. 3rd ed. Artech House; 2005.
34. Schneider JB. *Understanding the finite-difference time-domain method*. School of Electrical Engineering and Computer Science, Washington State University; 2010:28.
35. Alipour-Banaei H, Serajmohammadi S, Mehdizadeh F, Andalib A. Band gap properties of two-dimensional photonic crystal structures with rectangular lattice. *J Opt Commun*. 2015;36(2):109-114.

How to cite this article: Mönkölä S, Räty J. Discrete exterior calculus for photonic crystal waveguides. *Int J Numer Methods Eng*. 2022;1-20. doi: 10.1002/nme.7144